ACSNANO
www.acsnano.org

ARTICLE

Two-Dimensional $CH_3NH_3PbI_3$ Perovskite: Synthesis and Optoelectronic Application

Jingying Liu,[†,¶] Yunzhou Xue,[†,‡,¶] Ziyu Wang,[†,¶] Zai-Quan Xu,[†] Changxi Zheng,[§] Bent Weber,[⊥] Jingchao Song,[†] Yusheng Wang,[‡] Yuerui Lu,[∥] Yupeng Zhang,*[,†] and Qiaoliang Bao*[,‡,†]

[†]Department of Materials Science and Engineering, [§]Department of Civil Engineering, and [⊥]School of Physics, Monash University, Wellington Road, Clayton, Victoria 3800, Australia

[‡]Institute of Functional Nano and Soft Materials (FUNSOM), Jiangsu Key Laboratory for Carbon-Based Functional Materials and Devices, and Collaborative Innovation Center of Suzhou Nano Science and Technology, Soochow University, Suzhou 215123, People's Republic of China

[∥]Research School of Engineering, College of Engineering and Computer Science, the Australian National University, Canberra, ACT 2601, Australia

Supporting Information

ABSTRACT: **Hybrid organic–inorganic perovskite materials have received substantial research attention due to their impressively high performance in photovoltaic devices. As one of the oldest functional materials, it is intriguing to explore the optoelectronic properties in perovskite after reducing it into a few atomic layers in which two-dimensional (2D) confinement may get involved. In this work, we report a combined solution process and vapor-phase conversion method to synthesize 2D hybrid organic–inorganic perovskite (*i.e.*, $CH_3NH_3PbI_3$) nanocrystals as thin as a single unit cell (~1.3 nm). High-quality 2D perovskite crystals have triangle and hexagonal shapes, exhibiting tunable photoluminescence while the thickness or composition is changed. Due to the high quantum efficiency and excellent photoelectric properties in 2D perovskites, a high-performance photodetector was demonstrated, in which the current can be enhanced significantly by shining 405 and 532 nm lasers, showing photoresponsivities of 22 and 12 AW^{-1} with a voltage bias of 1 V, respectively. The excellent optoelectronic properties make 2D perovskites building blocks to construct 2D heterostructures for wider optoelectronic applications.**

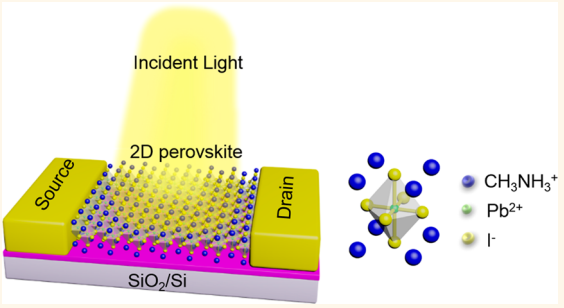

KEYWORDS: *two-dimensional material, hybrid organic–inorganic perovskite, optoelectronic, photodetector*

The rapid progress in graphene[1] and the methodology developed in preparing ultrathin atomic layer materials[2] has led to exploration of other two-dimensional (2D) materials such as hexagonal boron nitride (h-BN),[3] transition metal dichalcogenides (TMDs),[4−6] and black phosphorus,[7,8] *etc.* In particular, 2D semiconductor materials have received significant attention due to strong quantum confinement and the sizable band gap in these materials, which are desired for many optoelectronic applications. Recently, hybrid organic–inorganic perovskites described by the formula ABX_3 ($A = CH_3NH_3^+$; $B = Pb^{2+}$ or Sn^{2+}; and $X = Cl^-$, I^-, and/or Br^-) have been intensively studied as an emerging material for solar energy harvesting due to impressive power conversion efficiency over 20%.[9−12] These materials have many interesting properties such as intrinsic ambipolar transport, high optical absorption coefficient in visible spectral range, changeable band gap, high quantum efficiency, and a long carrier diffusion length,[13,14] showing promising potential for optoelectronic and photonic devices such as solar cells,[15,16] photodetectors,[17] light-emitting diodes,[18] field-effect transistors,[19] waveguides,[20] as well as nanolasers.[21] It is intriguing to investigate the optoelectronic properties in 2D perovskite after reducing it into single- and few-unit-cell-thick crystals in which 2D quantum wells are exposed and the electronic coupling between the top and bottom layers may be varied.

A variety of methods have been developed to synthesize the perovskite from polycrystalline film to bulk single crystal.[14] However, the introduction of many defects and grain boundaries in three-dimensional (3D) bulk perovskite is unavoidable,[22] which could degrade the optoelectronic properties. Niu *et al.*[23] successfully produced ultrathin 2D perovskite flakes using micromechanical exfoliation as used for graphene and found distinct exciton properties in thick and thin regions. Xiong and co-workers[24,25] reported the synthesis of perovskite

Received: December 11, 2015
Accepted: February 24, 2016

ACS Publications © XXXX American Chemical Society

DOI: 10.1021/acsnano.5b07791
ACS Nano XXXX, XXX, XXX−XXX

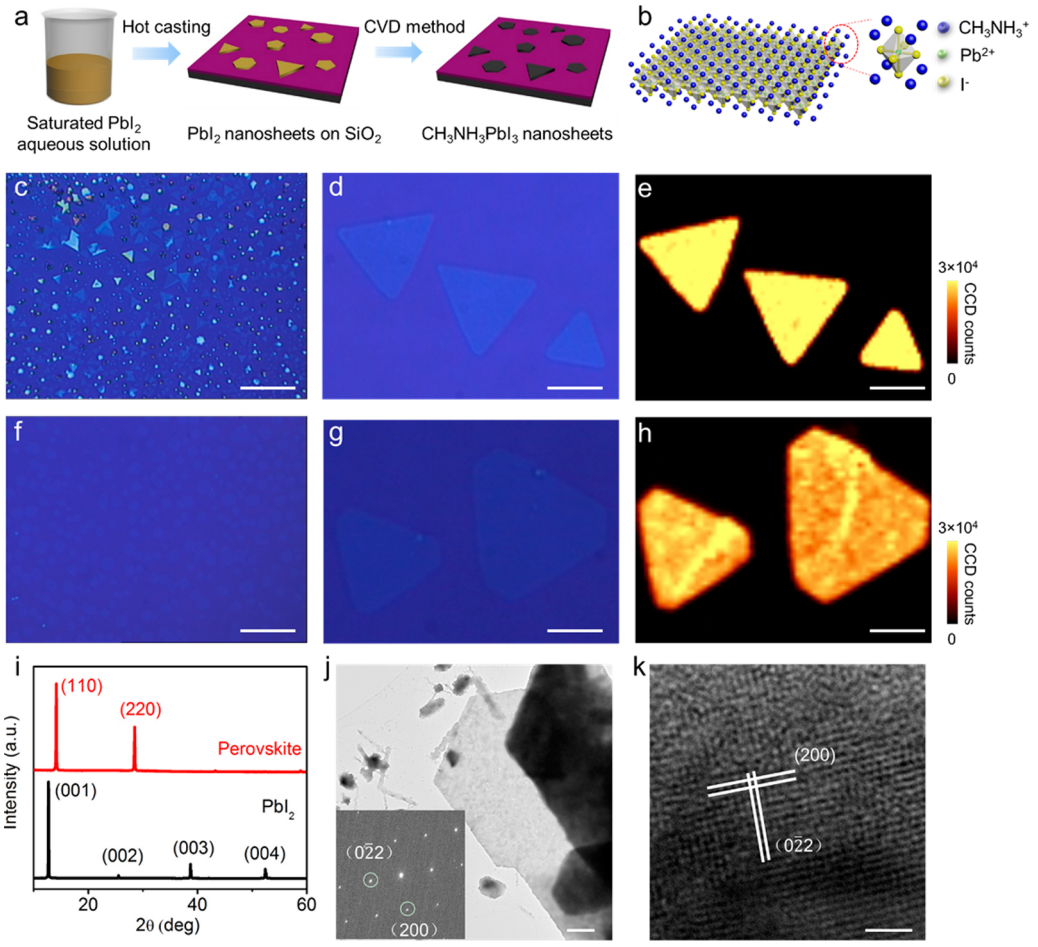

Figure 1. (a) Schematic illustration of solution process to fabricate 2D PbI_2 nanosheets and vapor-phase conversion process to transfer PbI_2 into 2D $CH_3NH_3PbI_3$ perovskite nanosheets. (b) Crystal structure of single-unit-cell-thick 2D $CH_3NH_3PbI_3$ perovskite. (c) Optical image of 2D $CH_3NH_3PbI_3$ nanosheets synthesized by hot casting (>90 °C) and vapor-phase conversion. Scale bar: 10 μm. (d) High-magnification optical image of 2D $CH_3NH_3PbI_3$ nanosheets. Scale bar: 4 μm. (e) PL mapping image of 2D $CH_3NH_3PbI_3$ nanosheets shown in (d). Scale bar: 4 μm. (f) Optical image of 2D $CH_3NH_3PbI_3$ nanosheets synthesized by hot casting (<90 °C) and vapor-phase conversion. Scale bar: 10 μm. (g) High-magnification optical image of 2D $CH_3NH_3PbI_3$ nanosheets. Scale bar: 4 μm. (h) PL mapping image of 2D $CH_3NH_3PbI_3$ nanosheets shown in (g). Scale bar: 4 μm. (i) XRD patterns of PbI_2 nanosheets and converted $CH_3NH_3PbI_3$ nanosheets. (j) Low-magnification TEM image of a 2D $CH_3NH_3PbI_3$ nanosheet. Scale bar: 0.5 μm. The inset shows an electron diffraction pattern of the nanosheet. (k) High-resolution TEM image of a 2D $CH_3NH_3PbI_3$ nanosheet. Scale bar: 2 nm.

nanoplatelets with a thickness from dozens to several hundred nanometers by using the chemical vapor deposition (CVD) method, bringing us a step closer to produce ultrathin perovskite. Liao *et al.*[26] reported a one-step solution self-assembly method to prepare a single-crystalline square microdisk of $CH_3NH_3PbI_3$ with a thickness of about 500 nm. However, how to synthesize ultrathin 2D perovskite with a thickness down to a single unit cell is still challenging because of the poor chemical stability, fast crystallization rate, and the intrinsically non-van der Waals-type 3D characteristics of perovskite. The uncontrolled growth of perovskite will produce grains with random crystal size and large morphological variations, leading to very different photovoltaic performance in the resulting devices, which represents one of the major barriers for practical applications.[27] In this regard, the realization of 2D perovskite with several unit cells (less than 10 nm), even with single-unit-cell thickness, will contribute to a comprehensive understanding of the intrinsic physical properties, especially charge carrier behaviors, which are the basis of perovskite-based functional optoelectronic devices. Very recently, Dou and co-workers[28] reported the solution-phase growth of single- and few-unit-cell-thick 2D hybrid perovskites of $(C_4H_9NH_3)_2PbBr_4$ with well-defined square shape and large size. They also found that the color tuning of the photoluminescence (PL) spectrum could be achieved by changing the sheet thickness as well as composition. However, the one-step solution process limits the composition modification of $(C_4H_9NH_3)_2PbBr_4$ perovskite somewhat, making it difficult to obtain 2D $CH_3NH_3PbX_3$ (X = Cl^-, Br^-, or I^-) perovskites, which have better photovoltaic performance and a broader range of applications.[29] Synthesis and device application of 2D $CH_3NH_3PbX_3$ perovskite are thus of strategic interest.

In this work, we demonstrate the preparation of 2D $CH_3NH_3PbX_3$ perovskites as thin as a single unit cell, using a combined solution process and vapor-phase conversion method. In particular, the 2D PbI_2 was used as the template, resulting in the growth of a non-van der Waals-type 2D perovskite (*i.e.*, $CH_3NH_3PbI_3$). This two-step process is highly versatile to produce many different 2D perovskites pertaining to the same structural framework through the intercalation of different organic cations or halogen anions. Owing to the character of single- or few-unit-cell thickness, it is interesting to

DOI: 10.1021/acsnano.5b07791
ACS Nano XXXX, XXX, XXX–XXX

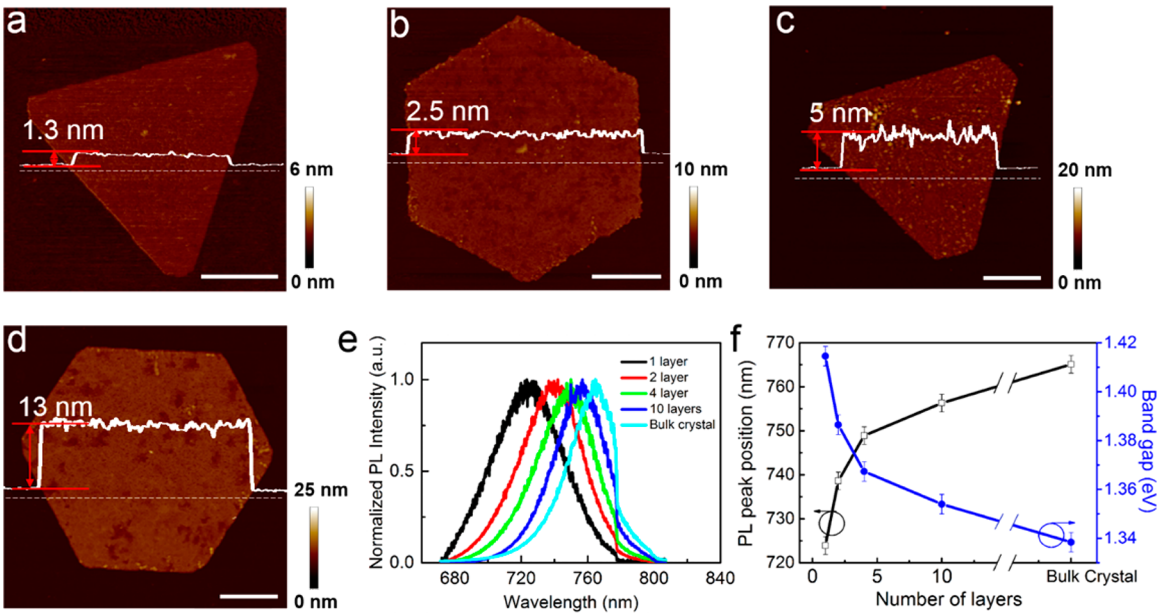

Figure 2. (a–d) AFM topography images of 2D $CH_3NH_3PbI_3$ nanosheets with different thicknesses. Scale bars: 2 μm. (a) Single-layer $CH_3NH_3PbI_3$. The height profile indicates a thickness of 1.3 nm. (b) Two-layer $CH_3NH_3PbI_3$. The height profile indicates a thickness of 2.5 nm. (c) Four-layer $CH_3NH_3PbI_3$. The height profile indicates a thickness of 5.0 nm. (d) Ten-layer $CH_3NH_3PbI_3$. The height profile indicates a thickness of 13.0 nm. (e) Normalized PL spectra of 2D perovskite nanosheets with different thicknesses. (f) PL peak position and energy gap as a function of the number of unit cells in perovskite.

find that the 2D perovskite exhibits high PL quantum yield, unique band structure compared to the bulk crystal, and excellent photodetection performance.

RESULTS AND DISCUSSION

The 2D hybrid organic–inorganic perovskite nanosheets were prepared by a two-step method, as schematically shown in Figure 1a. This method involves casting saturated PbI_2 aqueous solution onto a substrate and subsequently heating the substrate at an elevated temperature, during which 2D PbI_2 nanosheets will nucleate. Subsequently, the 2D $CH_3NH_3PbI_3$ perovskite nanosheets were formed by intercalating the CH_3NH_3I molecules into the interval sites of PbI_6 octahedron layers. The resulting $CH_3NH_3PbI_3$ perovskite still maintains the 2D lamellar structure, indicating good morphology retention after vapor-phase conversion. It is found that the heating temperature in the solution process is crucial to affect the nucleation and growth of 2D PbI_2 nanosheets because the number of nucleation sites is controlled by temperature. When the temperature is greater than 90 °C, the crystal growth rate is much higher than the nucleation rate, and a large amount of thick PbI_2 crystals will precipitate on the substrate. Nevertheless, some triangular or hexagonal 2D PbI_2 nanosheets with single-crystalline nature can still be observed at a particular region on the substrate (Figure 1c,d) upon the concentration change of PbI_2 solution during drying in about 100 s. The 2D structure indicates that the out-of-plane growth rate along the *c*-axis is much lower than that of the in-plane one. This is because of different surface energies along different directions; that is, generally lower surface energy is expected along the in-plane direction and thus leads to a faster growth rate.[30] Due to the high-temperature growth process, the crystal quality is high, resulting in high PL quantum yield after converting PbI_2 into $CH_3NH_3PbI_3$. The high and uniform PL intensity over the whole $CH_3NH_3PbI_3$ crystal (Figure 1e) suggests that the sample maintains good uniformity and continuity after the conversion process. By contrast, low temperature (<90 °C) in the hot casting process could increase the quantity of the crystal nucleus and inhibit the crystal growth rate to achieve large-scale production of 2D PbI_2 nanosheets (Figure 1f,g). However, the low-temperature growth process always lasts for 30 min to 1 h. It should be noted that the PbI_2 is also unstable in H_2O. During the slow growth process at low temperature, there is a competitive relationship between the PbI_2 crystal growth and redissolution, which will affect the crystal quality inevitably, leading to relatively low PL intensity (Figure 1h) in resulting $CH_3NH_3PbI_3$ nanosheets. The corresponding AFM image (Supporting Information, Figure S1) of a perovskite nanosheet reveals jagged edges, which is evidence of redissolution. Compared with CVD methods, the solution process can produce PbI_2 crystals with well-controlled morphologies. The PbI_2 and subsequent $CH_3NH_3PbI_3$ nanowires, nanobelts, and nanosheets with different diameters and thicknesses can be obtained by controlling the evaporation rate of solvent, which is associated with solvent type and the temperature of solvent and substrate (see Figure S2 in Supporting Information).

X-ray diffraction (XRD) and transmission electron microscopy (TEM) were used to investigate the microstructure of PbI_2 and $CH_3NH_3PbI_3$ nanosheets. Figure 1i shows the XRD results of PbI_2 and $CH_3NH_3PbI_3$ nanosheets grown on glass substrates. The XRD pattern of PbI_2 shows four dominant diffraction peaks at 12.8, 25.6, 38.5, and 52.3°, which can be assigned to the (001), (002), (003), and (004) facets, respectively, of the 2H hexagonal crystalline structure. After the CVD conversion process, two new peaks at 14.1 and 28.5° are observed, which can be indexed to (110) and (220) facets, respectively, of the tetragonal structure of perovskite. It should be noted that the diffraction peaks of PbI_2 disappeared, suggesting a complete conversion of PbI_2 into perovskite crystals. More interestingly, a few XRD peaks such as (112), (211), (310), and (224), which normally appear in solution-

DOI: 10.1021/acsnano.5b07791
ACS Nano XXXX, XXX, XXX–XXX

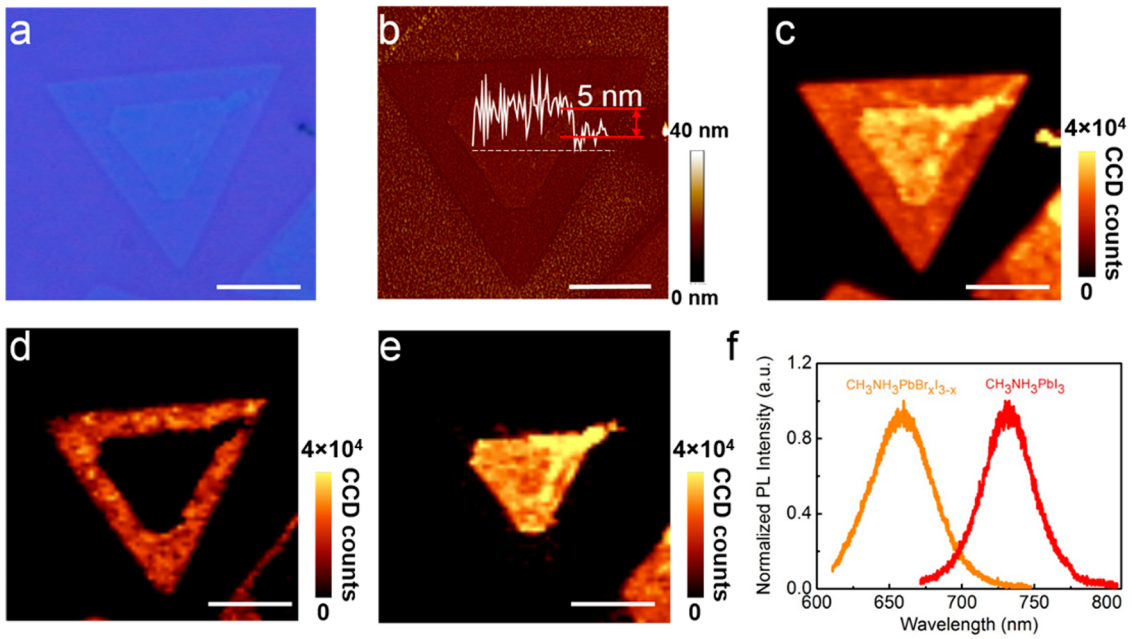

Figure 3. (a–c) Optical, AFM, and PL mapping images of the as-grown $CH_3NH_3PbI_3$ nanosheet with different thicknesses (thin $CH_3NH_3PbI_3$ sheet with a thicker region at the center). Scale bar: 10 μm. (d) PL mapping image of the 2D heterostructure integrated by a PL peak at 660 nm. Scale bar: 10 μm. (e) PL mapping image of the 2D heterostructure integrated by a PL peak at 730 nm. Scale bar: 10 μm. (d) Normalized PL spectra measured from central (red trace) and peripheral (orange trace) regions of the 2D heterostructure.

based approaches (Supporting Information, Figure S3), were not observed in as-produced 2D $CH_3NH_3PbI_3$ sheets, indicating a well-preferred crystal orientation in our samples. The electron diffraction pattern in Figure 1j further verifies those two facets, which are distinct from those of PbI_2 (Supporting Information, Figure S4). The high-resolution TEM image reveals clear lattice fringes of (200) and ($0\bar{2}2$) facets (Figure 1k), indicating a complete conversion into the perovskite structure. It should be noted that the perovskite was sensitive to electron beam or laser irradiation, as PbI_2 reflections are observed in the diffraction patterns under long irradiation times (Supporting Information, Figure S5). This is due to localized loss of CH_3NH_3I under electron beam or laser irradiation, recovering a small region into PbI_2. The rewritable characteristic under electron beam or laser will make this type of perovskite a promising candidate for fabricating novel functional devices, which needs further investigation. Density functional theory calculations were performed (Supporting Information, Figure S6) to investigate the structure transformation from a hexagonal to a monoclinic system when the CH_3NH_3I molecules were intercalated into the interval sites of PbI_6 octahedrons layers. Due to the complete conversion of PbI_2 into $CH_3NH_3PbI_3$ perovskite, the length of the *c*-axis could be increased, and the shear stress in the *a*–*b* plane will be introduced, which changes the γ angle. As a result, the lattice changes from monoclinic to tetragonal structure.

The topography and thickness of 2D $CH_3NH_3PbI_3$ perovskite nanosheets with different numbers of layers were investigated by AFM, as shown in Figure 2a–d. It is found that the surface of 2D $CH_3NH_3PbI_3$ nanosheets becomes relatively rough compared to that of the PbI_2 nanosheets, due to the adsorption of CH_3NH_3I molecules on the surfaces. AFM topography indicates a surface roughness of 0.2–1.0 nm. The height profiles depict perovskite thicknesses of 1.3, 2.5, 5.0, and 13 nm, corresponding to 1, 2, 4, and 10 unit cells, respectively. The thickness of single-unit-cell $CH_3NH_3PbI_3$ is smaller than that of single-unit-cell $(C_4H_9NH_3)_2PbBr_4$ because of the smaller radius of the $CH_3NH_3^+$ ion. To the best of our knowledge, this is the first report on the synthesis of $CH_3NH_3PbX_3$ perovskite with 2D structure, which may show unique optical and electrical properties.

In order to investigate the optical properties of 2D perovskite nanosheets with different thicknesses, PL spectroscopy measurements were implemented under 532 nm laser excitation, as shown in Figure 2e,f. Both bulk crystals and 2D sheets with different thicknesses exhibit high quantum efficiency in terms of PL yield. However, the PL peaks shift to shorter wavelength gradually when decreasing the perovskite thickness. For the perovskite with single-unit-cell thickness, the PL peak is located around 720 nm. As reported by Dou *et al.*, the shift of PL emission for the ultrathin 2D perovskite sheets is probably induced by the lattice expansion; that is, the structural relaxation of the in-plane crystal lattice could increase the optical band gap.[28] It is interesting to find that the change of band gap in 2D $CH_3NH_3PbI_3$ is more pronounced than that of 2D $(C_4H_9NH_3)_2PbBr_4$ reported in ref 28. Generally, the electronic structure of hybrid organic–inorganic perovskite compounds (ABX_3) is governed by the B–X bond of the inorganic framework.[31,32] Although A cation does not directly affect the electrical structure, a large A cation can cause distortion of the B–X bonds, thus adversely affecting symmetry. While smaller A cations are intercalated into the interval sites of PbI_6 octahedrons layers, the B–X bonds undergo compression and the A–X bonds undergo tension to compensate for the excess space. Conversely, in the case of larger A cations, a higher degree of symmetry will be induced, resulting in a more stable electrical structure.[29] As a result, a broader tuning wavelength could be achieved for 2D $CH_3NH_3PbX_3$ because the radius of the $CH_3NH_3^+$ ion is much smaller than that of $(C_4H_9NH_3)_2^+$. Furthermore, there is no PL peak position shift between these crystals with different shapes (Supporting Information, Figure S7).

DOI: 10.1021/acsnano.5b07791
ACS Nano XXXX, XXX, XXX–XXX

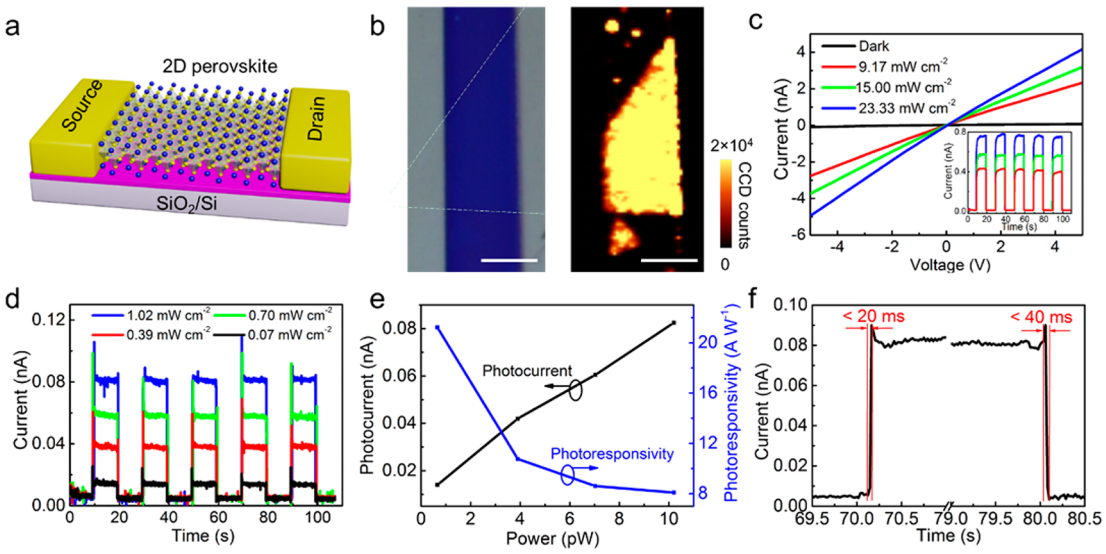

Figure 4. (a) Schematic image of a transistor device based on 2D perovskite. (b) Optical (left) and corresponding PL mapping (right) images of the 2D perovskite device. Scale bars: 10 μm. (c) $I-V$ curves of the 2D perovskite-based device under the irradiation of natural light with different power. Inset: Time-dependent photocurrent measurement over five on−off periods of operation under different power of natural light with a voltage bias of 1 V. (d) Time-dependent photocurrent measurement on the 2D perovskite phototransistor under the different power of a 405 nm laser with a voltage bias of 1 V. (e) Photocurrent and photoresponsivity *versus* optical illumination power at a wavelength of 405 nm with a voltage bias of 1 V. (f) Temporal photocurrent response excited at 405 nm. The rise time (<20 ms) is defined as the time for the photocurrent to increase to 70% of the ON-state current. The fall time (<40 ms) is defined as the time for the photocurrent to decrease by 70% of the ON-state current.

One of the most interesting characteristics of hybrid organic−inorganic perovskite is that the halogen elemental composition could be substituted by reacting with different organic molecules, which could induce a changeable band structure and consequently tunable optical properties. In principle, it is easier for an anion to exchange in atomically thin perovskite crystal with exposed 2D quantum wells at the top and bottom surfaces. Figure S8 in the Supporting Information depicts the PL spectra of the as-synthesized 2D $CH_3NH_3PbI_3$ (red trace), $CH_3NH_3PbBr_xI_{3-x}$ (orange trace), and $CH_3NH_3PbBr_3$ (green trace) nanosheets at room temperature. The peaks of PL emission from $CH_3NH_3PbBr_3$, $CH_3NH_3PbBr_xI_{3-x}$ and $CH_3NH_3PbI_3$ nanosheets appear at approximately 535, 660, and 730 nm, respectively, consistent with the previous report.[18] However, the 2D nanosheets have obvious blue-shifted peaks due to the 2D quantum confinement effect. In comparison to $CH_3NH_3PbI_3$ and $CH_3NH_3PbBr_3$, $CH_3NH_3PbBr_xI_{3-x}$ has broadened and blue-shifted PL emission, possibly due to the existence of alloying composition.

An in-plane heterostructure consisting of $CH_3NH_3PbI_3$ and $CH_3NH_3PbBr_xI_{3-x}$ was produced by controllably annealing the as-grown $CH_3NH_3PbI_3$ nanosheet with different thickness (thin $CH_3NH_3PbI_3$ sheet with a thicker region at the center) in excess CH_3NH_3Br vapor environment. The optical, AFM, and PL mapping images for the as-grown $CH_3NH_3PbI_3$ nanosheet are shown in Figure 3a−c, revealing the thickness difference between the center and edge regions. While the thin $CH_3NH_3PbI_3$ sheet with a thicker region at the center reacted with CH_3NH_3Br, anion exchange first occurred at the thin edges of the $CH_3NH_3PbI_3$ perovskite nanosheet then toward the thicker region at the center. This is because the iodide ions in the peripheral region can be easily replaced with a bromide ion, whereas the chemical composition in the central region does not change. Figure 3d−f reveals distinct PL emission from the central region and the peripheral region, which are centered at 730 and 660 nm, and in good agreement with the near band-edge emission from $CH_3NH_3PbI_3$ and $CH_3NH_3PbBr_xI_{3-x}$, respectively. Interestingly, the PL mapping measurements indicate that there is no apparent overlap or gap between the $CH_3NH_3PbI_3$ and $CH_3NH_3PbBr_xI_{3-x}$ regions, suggesting that $CH_3NH_3PbI_3$ (inner triangle) and $CH_3NH_3PbBr_xI_{3-x}$ (surrounding region) are laterally connected with well-defined interface.

We further fabricate a field-effect transistor to evaluate the electronic and photoelectric properties of a 2D $CH_3NH_3PbI_3$ sheet. The perovskite-based transistor device with a back gate is schematically shown in Figure 4a. In order to prevent doping by contamination, a lithography-free technique with electrode materials with a patterned Si_3N_4 shadow mask was used to fabricate clean devices. Figure 4b shows the optical and PL mapping images of the transistor device based on single-unit-cell perovskite. It is notable that the source−drain current (I_{D-S}) is very small (about 10^{-12} A, close to nonconductive) in dark conditions, and the I_{D-S} could not be tuned by gate voltage, which is very different from the bulk materials. However, even under the illumination of a dim light, the current of the 2D perovskite-based device could be significantly enhanced, promising great potential as an effective photodetector. Typical $I-V$ curves of the 2D perovskite-based device under the irradiation of natural light with different power are shown in Figure 4c. Clearly, $I-V$ curves present linear dependence on the applied bias, indicating ohmic contact between perovskite and gold electrodes. The ratio of photocurrent to dark current can reach up to 2 orders of magnitude (Figure 4c, inset), which is attributed to strong light−matter interaction as well as broad-band light-harvesting capability in a single-unit-cell perovskite nanosheet. However, when the 2D perovskite-based device was illuminated by a weak laser (405 or 532 nm, unfocused, the effective power <10 pw), the hysteresis can be observed in $I-V$ curves; that is, the

DOI: 10.1021/acsnano.5b07791
ACS Nano XXXX, XXX, XXX−XXX

current depends on the direction of the voltage sweeping between the source and drain electrodes (Supporting Information, Figure S9). It is supposed to be related to the poling effect in $CH_3NH_3PbI_3$.[33] Nevertheless, the 2D perovskite-based photodetector is sensitive to a broad-band light from the ultraviolet to the entire visible spectral range. Time-dependent photocurrent was measured under the illumination of natural light (inset of Figure 4c), a 405 nm laser (Figure 4d), and a 532 nm laser (Supporting Information, Figure S10), indicating effective optical switching. The photoresponsivities of the phototransistor with a voltage bias of 1 V were calculated to be 22 AW^{-1} under a 405 nm laser and 12 AW^{-1} under a 532 nm laser. These are much higher than that of photodetectors based on bulk perovskite film (3 AW^{-1})[34] but slightly lower than perovskite microplate crystals (40 AW^{-1}).[35] As one of the key figures of merit, the relatively faster response time can also naturally broaden the scope of the device application. It is found that the rise and decay times of the photodetector based on 2D $CH_3NH_3PbI_3$ nanosheets are shorter than 20 and 40 ms, respectively (Figure 4f), suggesting a much faster response time than photodetectors based on bulk films.[34] The results above show that the 2D perovskite device has excellent photoresponsivity and relatively fast response time for light detection, which affords the potential for application in optoelectronic switches and photodetectors.

CONCLUSION

In summary, we have successfully demonstrated a facile method to produce atomically thin 2D $CH_3NH_3PbX_3$ (X = Cl, Br, or I) perovskite nanosheets and heterostructure. The high-quality 2D perovskite crystals exhibit high PL quantum efficiency with broad wavelength tunability. The excellent optical and photoelectric properties make 2D perovskite a promising candidate for high-performance photodetectors. The realization of 2D perovskite with several-unit-cell (less than 10 nm) and even single-unit-cell thickness can open up exciting opportunities for the fundamental understanding of this type of materials and creation of a wide range of functional devices, ranging from photovoltaics and photodetectors to light-emitting diodes and laser diodes.

METHODS

The 2D $CH_3NH_3PbI_3$ perovskite nanosheets were prepared by two steps. First, saturated PbI_2 aqueous solution was prepared by dissolving 1 mg of PbI_2 powder (Sigma-Aldrich) in 1 mL of DI water and heated at 90 °C for 1 h. Then the solution was drop-casted on the SiO_2/Si substrate and heated at a temperature from 30 to 180 °C. The 2D PbI_2 nanosheets nucleate on the substrate during drying. In the second step, the CH_3NH_3I powder, which was synthesized according to previous work,[36] was placed at the center of a CVD furnace while the as-grown 2D PbI_2 nanosheets on the silicon oxide substrate were mounted downstream of the apparatus. The central heating zone was increased to 120 °C under low-pressure conditions (40−50 Torr) and maintained for 40 min to 4 h. Ar and H_2 were introduced into the quartz tube as carrier gases with flow rates of 35 and 15 sccm, respectively, during the whole vapor conversion process. The furnace was then naturally cooled to room temperature with the cover closed at a cooling rate of 5 °C/min. The 2D $CH_3NH_3PbBr_xI_{3-x}$ and $CH_3NH_3PbBr_3$ nanosheets were synthesized by controllably annealing as-grown $CH_3NH_3PbI_3$ nanosheets in an excess CH_3NH_3Br vapor environment at 120 °C under low pressure (40−50 Torr) with different holding times (from 15 min to 2 h). Different annealing times result in complete or partial halogen element substitution.

The morphologies and topography of the 2D $CH_3NH_3PbI_3$ perovskite nanosheets were characterized using optical microscopy and atomic force microscopy (Bruker, Dimension Icon SPM). XRD experiments were conducted by a Philips X-ray diffractometer with Cu Kα radiation. The samples were scanned from 10 to 60° with a step size of 0.02°. The microstructure of the samples and electron diffraction pattern were characterized using a TEM microscope (FEI, Tecnai G2 F20). PL measurements were performed using a confocal microscope system (WITec, alpha 300R) with a 100× objective lens (NA = 0.9) in ambient conditions. We used 450 and 532 nm lasers to excite samples, which were placed on a piezo-crystal-controlled scanning stage. The spectra are collected using 600 lines/mm gratings with a spectral resolution of <0.09 nm. To avoid sample damage, low laser power (5 μW) was applied during the measurements. The exposure time was 0.01 s, and the accumulation number was 10. Many different locations of the sample were tested, and an average was made to conclude the PL peak position of each sample.

The 2D $CH_3NH_3PbI_3$-based phototransistor devices were fabricated on a SiO_2/Si substrate. The electrodes were patterned using parallel Si_3N_4 grids as a shadow mask to define the deposition region, followed by electron beam deposition of Ti/Au (5/50 nm) in vacuum with a chamber pressure of $<6 \times 10^{-6}$ Torr. The channel length between the source and drain electrodes was around 10 μm. The source−drain current as a function of bias voltage upon an unfocused 405 nm laser, a 532 nm laser, and natural light illumination was recorded by a source meter unit (Agilent, B2902A).

ASSOCIATED CONTENT

Supporting Information

The Supporting Information is available free of charge on the ACS Publications website at DOI: 10.1021/acsnano.5b07791.

Additional figures and experimental details (PDF)

AUTHOR INFORMATION

Corresponding Authors

*E-mail: yupeng.zhang@monash.edu.

*E-mail: qlbao@suda.edu.cn.

Author Contributions

¶J.L., Y.X., and Z.W. contributed equally to this work.

Notes

The authors declare no competing financial interest.

ACKNOWLEDGMENTS

This work was supported by ARC DECRA (DE120101569) and DSI top-up grant, DP (DP140101501), Engineering Seed Fund in Monash University. J.L. and Z.W. acknowledge support from the MCATM scholarship at Monash University. Q.B. also acknowledges the support from 863 Program (Grant No. 2013AA031903), the youth 973 program (2015CB932700), the National Natural Science Foundation of China (Grant Nos. 51222208, 51290273, 91433107), China Postdoctoral Science Foundation (2014M550303), the Priority Academic Program Development of Jiangsu Higher Education Institutions, and Collaborative Innovation Center of Suzhou Nano Science and Technology. This work was performed in part at the Melbourne Centre for Nanofabrication (MCN) in the Victorian Node of the Australian National Fabrication Facility (ANFF).

REFERENCES

(1) Novoselov, K. S.; Geim, A. K.; Morozov, S. V.; Jiang, D.; Zhang, Y.; Dubonos, S. V.; Grigorieva, I. V.; Firsov, A. A. Electric Field Effect in Atomically Thin Carbon Films. *Science* **2004**, *306*, 666−669.

(2) Novoselov, K. S.; Jiang, D.; Schedin, F.; Booth, T. J.; Khotkevich, V. V.; Morozov, S. V.; Geim, A. K. Two-Dimensional atomic crystals. *Proc. Natl. Acad. Sci. U. S. A.* **2005**, *102*, 10451−10453.

DOI: 10.1021/acsnano.5b07791
ACS Nano XXXX, XXX, XXX−XXX

(3) Dean, C. R.; Young, A. F.; Meric, I.; Lee, C.; Wang, L.; Sorgenfrei, S.; Watanabe, K.; Taniguchi, T.; Kim, P.; Shepard, K. L.; Hone, J. Boron Nitride Substrates for High-Quality Graphene Electronics. *Nat. Nanotechnol.* **2010**, *5*, 722−726.
(4) Xu, Z. Q.; Zhang, Y.; Lin, S.; Zheng, C.; Zhong, Y. L.; Xia, X.; Li, Z.; Sophia, P. J.; Fuhrer, M. S.; Cheng, Y. B.; Bao, Q. Synthesis and Transfer of Large-Area Monolayer WS_2 Crystals: Moving Toward the Recyclable Use of Sapphire Substrates. *ACS Nano* **2015**, *9*, 6178−6187.
(5) Chen, C.; Qiao, H.; Xue, Y.; Yu, W.; Song, J.; Lu, Y.; Li, S.; Bao, Q. Growth of Large-Area Atomically Thin MoS_2 Film *via* Ambient Pressure Chemical Vapor Deposition. *Photonics Res.* **2015**, *3*, 110−114.
(6) Chen, C.; Qiao, H.; Lin, S.; Man Luk, C.; Liu, Y.; Xu, Z.; Song, J.; Xue, Y.; Li, D.; Yuan, J.; Yu, W.; Pan, C.; Ping Lau, S.; Bao, Q. Highly Responsive MoS_2 Photodetectors Enhanced by Graphene Quantum Dots. *Sci. Rep.* **2015**, *5*, 11830.
(7) Mu, H.; Lin, S.; Wang, Z.; Xiao, S.; Li, P.; Chen, Y.; Zhang, H.; Bao, H.; Lau, S. P.; Pan, C.; Fan, D.; Bao, Q. Black Phosphorus−Polymer Composites for Pulsed Lasers. *Adv. Opt. Mater.* **2015**, *3*, 1447−1453.
(8) Xia, F.; Wang, H.; Xiao, D.; Dubey, M.; Ramasubramaniam, A. Two-dimensional Material Nanophotonics. *Nat. Photonics* **2014**, *8*, 899−907.
(9) Green, M. A.; Ho-Baillie, A.; Snaith, H. J. The Emergence of Perovskite Solar Cells. *Nat. Photonics* **2014**, *8*, 506−514.
(10) Heo, J. H.; Im, S. H.; Noh, J. H.; Mandal, T. N.; Lim, C. S.; Chang, J. A.; Lee, Y. H.; Kim, H.-j.; Sarkar, A.; Nazeeruddin, Md. K.; Gratzel, M.; Seok, S. I. Efficient Inorganic-Organic Hybrid Heterojunction Solar Cells Containing Perovskite Compound and Polymeric Hole Conductors. *Nat. Photonics* **2013**, *7*, 486−491.
(11) Burschka, J.; Pellet, N.; Moon, S. J.; Humphry-Baker, R.; Gao, P.; Nazeeruddin, M. K.; Gratzel, M. Sequential Deposition as a Route to High-Performance Perovskite-Sensitized Solar Cells. *Nature* **2013**, *499*, 316−319.
(12) Liu, M.; Johnston, M. B.; Snaith, H. J. Efficient Planar Heterojunction Perovskite Solar Cells by Vapour Deposition. *Nature* **2013**, *501*, 395−398.
(13) Stranks, S. D.; Eperon, G. E.; Grancini, G.; Menelaou, C.; Alcocer, M. J. P.; Leijtens, T.; Herz, L. M.; Petrozza, A.; Snaith, H. J. Electron-Hole Diffusion Lengths Exceeding 1 Micrometer in an Organometal Trihalide Perovskite Absorber. *Science* **2013**, *342*, 341−344.
(14) Dong, Q.; Fang, Y.; Shao, Y.; Mulligan, P.; Qiu, J.; Cao, L.; Huang, J. Electron-hole diffusion lengths > 175 μm in solution-grown $CH_3NH_3PbI_3$ single crystals. *Science* **2015**, *347*, 967−970.
(15) Kojima, A.; Teshima, K.; Shirai, Y.; Miyasaka, T. Organometal Halide Perovskites as Visible-Light Sensitizers for Photovoltaic Cells. *J. Am. Chem. Soc.* **2009**, *131*, 6050−6051.
(16) Snaith, H. J. Perovskites: The Emergence of a New Area for Low-Cost, High-Efficiency Solar Cells. *J. Phys. Chem. Lett.* **2013**, *4*, 3623−3630.
(17) Wang, Y.; Zhang, Y.; Lu, Y.; Xu, W.; Mu, H.; Chen, C.; Qiao, H.; Song, J.; Li, S.; Sun, B.; Cheng, Y. B.; Bao, Q. Hybrid Graphene−Perovskite Phototransistors with Ultrahigh Responsivity and Gain. *Adv. Opt. Mater.* **2015**, *3*, 1389−1396.
(18) Tan, Z. K.; Moghaddam, R. S.; Lai, M. L.; Docampo, P.; Higler, R.; Deschler, F.; Price, M.; Sadhanala, A.; Pazos, L. M.; Credgington, D.; Hanusch, F.; Bein, T.; Snaith, H. J.; Friend, R. H. Bright Light-Emitting Diodes Based on Organometal Halide Perovskite. *Nat. Nanotechnol.* **2014**, *9*, 687−692.
(19) Chin, X. Y.; Cortecchia, D.; Yin, J.; Bruno, A.; Soci, C. Lead Iodide Perovskite Light-Emitting Field-Effect Transistor. *Nat. Commun.* **2015**, *6*, 7383.
(20) Wang, Z.; Liu, J.; Xu, Z.-Q.; Xue, Y.; Jiang, L.; Song, J.; Huang, F.; Wang, Y.; Zhong, Y. L.; Zhang, Y.; Cheng, Y.-B.; Bao, Q. Wavelength-Tunable Waveguides Based on Polycrystalline Organic-Inorganic Perovskite Microwires. *Nanoscale* **2016**, DOI: 10.1039/C5NR06262D.
(21) Zhu, H.; Fu, Y.; Meng, F.; Wu, X.; Gong, Z.; Ding, Q.; Gustafsson, M. V.; Trinh, M. T.; Jin, S.; Zhu, X. Y. Lead Halide Perovskite Nanowire Lasers with Low Lasing Thresholds and High Quality Factors. *Nat. Mater.* **2015**, *14*, 636−642.
(22) Nie, W.; Tsai, H.; Asadpour, R.; Blancon, J. C.; Neukirch, A. J.; Gupta, G.; Crochet, J. J.; Chhowalla, M.; Tretiak, S.; Alam, M. A.; Wang, H.-L.; Mohite, A. D. High-Efficiency Solution-Processed Perovskite Solar Cells with Millimeter-Scale Grains. *Science* **2015**, *347*, 522−525.
(23) Niu, W.; Eiden, A.; Vijaya Prakash, G.; Baumberg, J. J. Exfoliation of Self-Assembled 2D Organic-Inorganic Perovskite Semiconductors. *Appl. Phys. Lett.* **2014**, *104*, 171111.
(24) Ha, S. T.; Liu, X.; Zhang, Q.; Giovanni, D.; Sum, T. C.; Xiong, Q. Synthesis of Organic−Inorganic Lead Halide Perovskite Nanoplatelets: Towards High-Performance Perovskite Solar Cells and Optoelectronic Devices. *Adv. Opt. Mater.* **2014**, *2*, 838−844.
(25) Zhang, Q.; Ha, S. T.; Liu, X.; Sum, T. C.; Xiong, Q. Room-Temperature Near-Infrared High-Q Perovskite Whispering-Gallery Planar Nanolasers. *Nano Lett.* **2014**, *14*, 5995−6001.
(26) Liao, Q.; Hu, K.; Zhang, H.; Wang, X.; Yao, J.; Fu, H. Perovskite Microdisk Microlasers Self-Assembled from Solution. *Adv. Mater.* **2015**, *27*, 3405−3410.
(27) Burschka, J.; Pellet, N.; Moon, S.-J.; Humphry-Baker, R.; Gao, P.; Nazeeruddin, M. K.; Gratzel, M. Sequential Deposition as a Route to High-Performance Perovskite-Sensitized Solar Cells. *Nature* **2013**, *499*, 316−319.
(28) Dou, L.; Wong, A. B.; Yu, Y.; Lai, M.; Kornienko, N.; Eaton, S. W.; Fu, A.; Bischak, C. G.; Ma, J.; Ding, T.; Ginsberg, N. S.; Wang, L. W.; Alivisatos, A. P.; Yang, P. Atomically Thin Two-Dimensional Organic-Inorganic Hybrid Perovskites. *Science* **2015**, *349*, 1518−1521.
(29) Chen, Q.; De Marco, N.; Yang, Y.; Song, T.-B.; Chen, C.-C.; Zhao, H.; Hong, Z.; Zhou, H.; Yang, Y. Under the Spotlight: The Organic−Inorganic Hybrid Halide Perovskite for Optoelectronic Applications. *Nano Today* **2015**, *10*, 355−396.
(30) Zheng, Z.; Liu, A.; Wang, S.; Wang, Y.; Li, Z.; Lau, W. M.; Zhang, L. *In Situ* Growth of Epitaxial Lead Iodide Films Composed of Hexagonal Single Crystals. *J. Mater. Chem.* **2005**, *15*, 4555−4559.
(31) Umebayashi, T.; Asai, K.; Kondo, T.; Nakao, A. Electronic Structures of Lead Iodide based Low-Dimensional Crystals. *Phys. Rev. B: Condens. Matter Mater. Phys.* **2003**, *67*, 155405.
(32) Umari, P.; Mosconi, E.; De Angelis, F. Relativistic GW calculations on $CH_3NH_3PbI_3$ and $CH_3NH_3SnI_3$ Perovskites for Solar Cell Applications. *Sci. Rep.* **2014**, *4*, 4467.
(33) Xiao, Z.; Yuan, Y.; Shao, Y.; Wang, Q.; Dong, Q.; Bi, C.; Sharma, P.; Gruverman, A.; Huang, J. Giant Switchable Photovoltaic Effect in Organometal Trihalide perovskite Devices. *Nat. Mater.* **2015**, *14*, 193−198.
(34) Hu, X.; Zhang, X.; Liang, L.; Bao, J.; Li, S.; Yang, W.; Xie, Y. High-Performance Flexible Broadband Photodetector Based on Organolead Halide Perovskite. *Adv. Funct. Mater.* **2014**, *24*, 7373−7380.
(35) Wang, G.; Li, D.; Cheng, H. C.; Li, Y.; Chen, C. Y.; Yin, A.; Zhao, Z.; Lin, Z.; Wu, H.; He, Q.; Ding, M.; Liu, Y.; Huang, Y.; Duan, X. Wafer-Scale Growth of Large Arrays of Perovskite Microplate Crystal for Functional Electronics and Optoelectronics. *Sci. Adv.* **2015**, *1*, e1500613.
(36) Xiao, M.; Huang, F.; Huang, W.; Dkhissi, Y.; Zhu, Y.; Etheridge, J.; Gray-Weale, A.; Bach, U.; Cheng, Y. B.; Spiccia, L. A Fast Deposition-Crystallization Procedure for Highly Efficient Lead Iodide Perovskite Thin-Film Solar Cells. *Angew. Chem.* **2014**, *126*, 10056−10061.

DOI: 10.1021/acsnano.5b07791
ACS Nano XXXX, XXX, XXX−XXX

Two-Dimensional $CH_3NH_3PbI_3$ Perovskite: Synthesis and Optoelectronic Application

Jingying Liu[†,||], Yunzhou Xue[‡,†,||], Ziyu Wang[†,||], Zai-Quan Xu[†], Changxi Zheng[§], Bent Weber[⊥], Jingchao Song[†], Yusheng Wang[‡], Yuerui Lu[#], Yupeng Zhang*[,†], and Qiaoliang Bao*[,‡,†]

[†]Department of Materials Science and Engineering, Monash University, Wellington Road, Clayton, Victoria 3800, Australia.

[‡]Institute of Functional Nano and Soft Materials (FUNSOM), Jiangsu Key Laboratory for Carbon-Based Functional Materials and Devices, and Collaborative Innovation Center of Suzhou Nano Science and Technology, Soochow University, Suzhou 215123, P. R. China.

[§]Department of Civil Engineering, Monash University, Clayton 3800, Victoria, Australia.

[⊥]School of Physics, Monash University, Monash 3800, Victoria, Australia.

[#]College of Engineering and Computer Science, Australian National University, Australia

[||]These authors contributed equally to this work.

*Address correspondence to qlbao@suda.edu.cn (Q. Bao), yupeng.zhang@monash.edu (Y. Zhang)

KEYWORDS: two-dimensional material, hybrid organic-inorganic perovskite, optoelectronics, photodetector

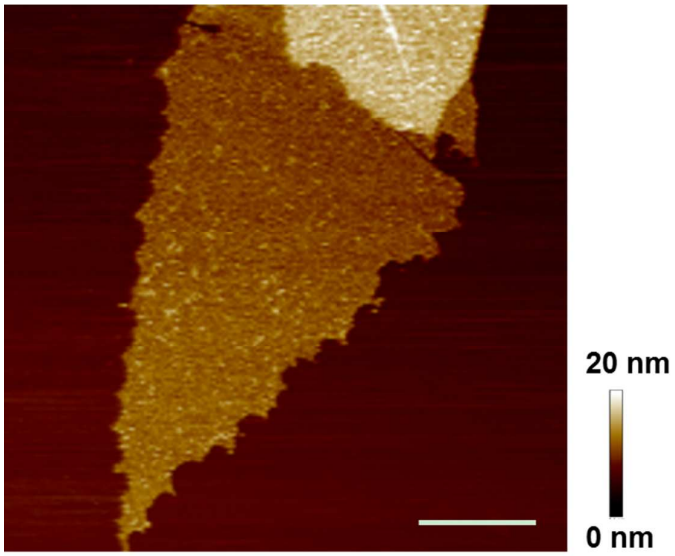

Figure S1. AFM topography image of 2D perovskite nanosheet produced by acombined low temperature solution process and CVD method. Scale bar: 2 μm.

The low temperature growth process always lasts for 30 mins to 1 hour. An important issue should to be noted is that the PbI_2 is also unstable in H_2O. During the slow growth process with low temperature, there is a competitive relationship between the PbI_2 crystal growth and re-dissolution, which will affect the crystal quality inevitably. The corresponding AFM image (Figure S1) for perovskite nanosheets reveals the re-dissolution clearly during the solution process, that is, the crystal exhibited the jagged edges.

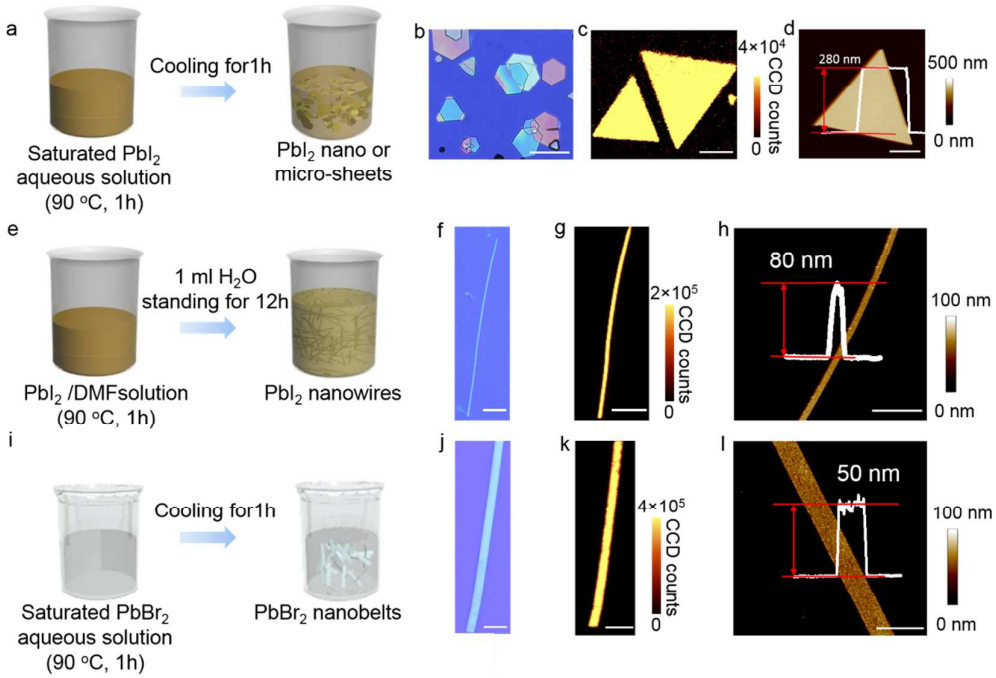

Figure S2. (a) Schematic illustration of solution process to fabricate thick PbI_2 nano or microsheets (thickness: 100-300 nm) (b) Optical image for perovskite microsheets. Scale bar: 5 μm. (c) PL mapping images for perovskite microsheets. Scale bar: 5 μm. (d) AFM images for perovskite microsheets. Scale bar: 5 μm. (e) Schematic illustration of solution process to fabricate PbI_2 nanowires. (f) Optical image for perovskite nanowires. Scale bar: 3 μm. (g) PL mapping images for perovskite nanowires. Scale bar: 3 μm. (h) AFM images for perovskite nanowires. Scale bar: 3 μm. (i) Schematic illustration of solution process to fabricate $PbBr_2$ nanobelts. (j) Optical image for perovskite nanobelts. Scale bar: 3 μm. (k) PL mapping images for perovskite nanobelts. Scale bar: 3 μm. (l) AFM images for perovskite nanobelts. Scale bar: 3 μm.

Compared with CVD method to synthesize the PbI_2 crystals, the morphology of PbI_2 crystals could be more controlled by our solution process. The PbI_2 and subsequent $CH_3NH_3PbI_3$ nanowires, nanobelts, and microsheets with different diameters and thicknesses could be obtained, as shown in Figure S2.

PbI_2 microsheets: Owing to the different solubility of PbI_2 in water at different temperatures, we developed a new crystallization method to prepare PbI_2 microsheets.

By inversing the growth temperature, the resulting PbI_2 microsheets with different diameters and thicknesses could be produced (Figure S2a-d).

PbI_2 nanowires: When dissolving 0.5g PbI_2 powder in N,N-dimethylmethanamide (DMF) solution at 90 ^oC for 1 hour, followed by the 12 hours standing time with deionized water added into the PbI_2/DMF solution, the PbI_2 nanowires will precipitate out (Figure S2e-h).

$PbBr_2$ nanobelts: Owing to the different solubility of $PbBr_2$ in water at different temperatures, by inversing the growth temperature, the resulting $PbBr_2$ nanobelts with different diameters and thicknesses could be produced (Figure S2i-l).

Similarly, the $CH_3NH_3PbI_3$ perovskites in different morphology can be formed through intercalating the CH_3NH_3I molecules into the interval sites of PbI_6 octahedrons layers by using CVD method.

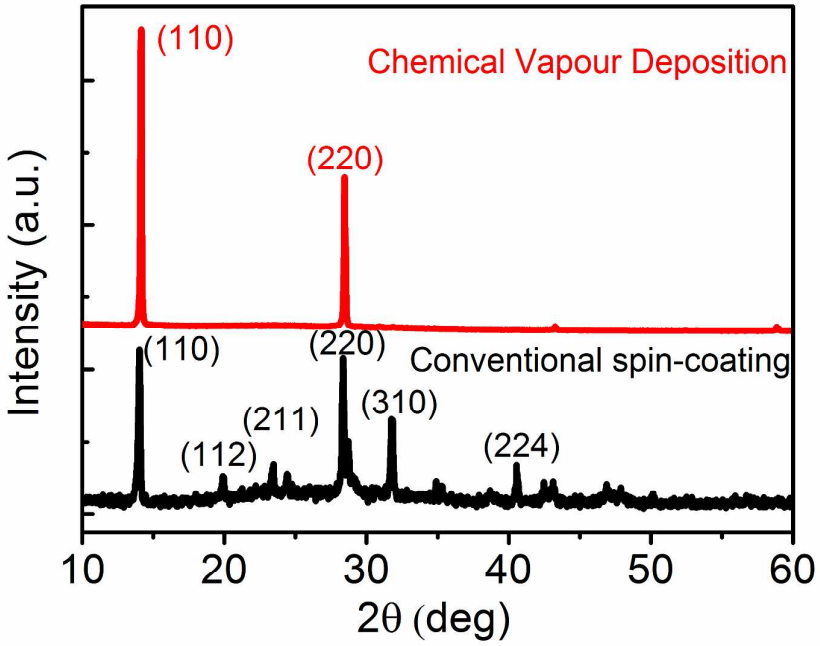

Figure S3 XRD patterns of $CH_3NH_3PbI_3$ perovskite produced by different methods. Red curve, perovskite nanosheets produced by a combined solution process and vapour phase conversion method. Black curve, $CH_3NH_3PbI_3$ film produced by a conventional two step spin-coating method.

XRD patterns are obtained from different samples produced by CVD process (2D nanosheets) and conventional spin-coating (polycrystalline thin film). The XRD patterns of perovskite nanosheets does not reveal the presence of other orientations: (112), (211), (310), and (224), indicating that the 2D $CH_3NH_3PbI_3$ nanosheets obtained by our method are highly crystallized and have preferred orientation on substrate.

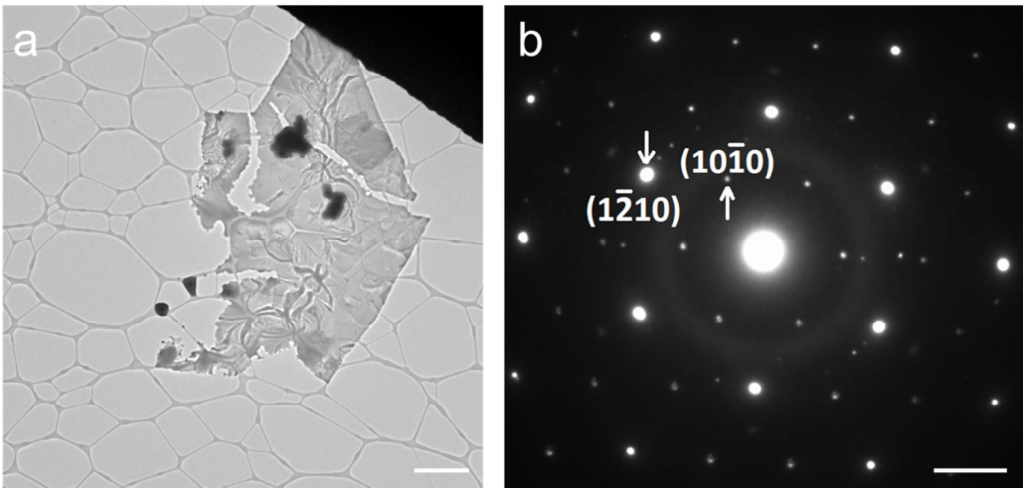

Figure S4 (a) Low magnification TEM image of a 2D PbI_2 nanosheet. Scale bar: 2 μm. (b) Selected-area electron diffraction pattern of PbI_2 nanosheet along the [0001] zone axis. Scale bar: 2 1/nm.

Figure S4a and b show the low magnification TEM image and the selected-area electron diffraction pattern taken from the as-grown PbI_2 nanosheet, indicating a highly crystalline PbI_2 with six-fold symmetric diffraction patterns.

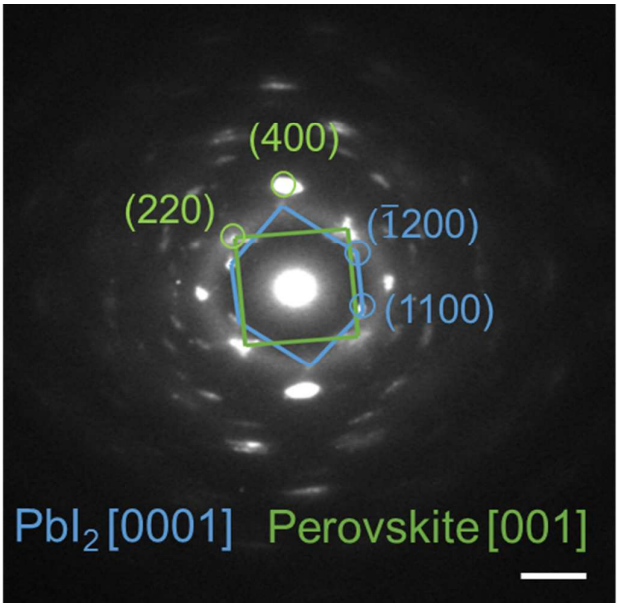

Figure S5 Electron diffraction pattern of 2D perovskite nanosheet under high energy electron beam irradiation. Scale bar: 2 1/nm.

It should be noted that the perovskite was sensitive to electron beam or laser irradiation, PbI_2 reflections are also evident in the diffraction patterns under the long irradiation time (Figure S5). This is due to localized loss of CH_3NH_3I under electron beam or laser irradiation, leaving small regions of PbI_2. The rewritable characteristic under electron beam or laser will make this type of perovskites promising candidates for fabricating novel functional devices, which needs further investigation.

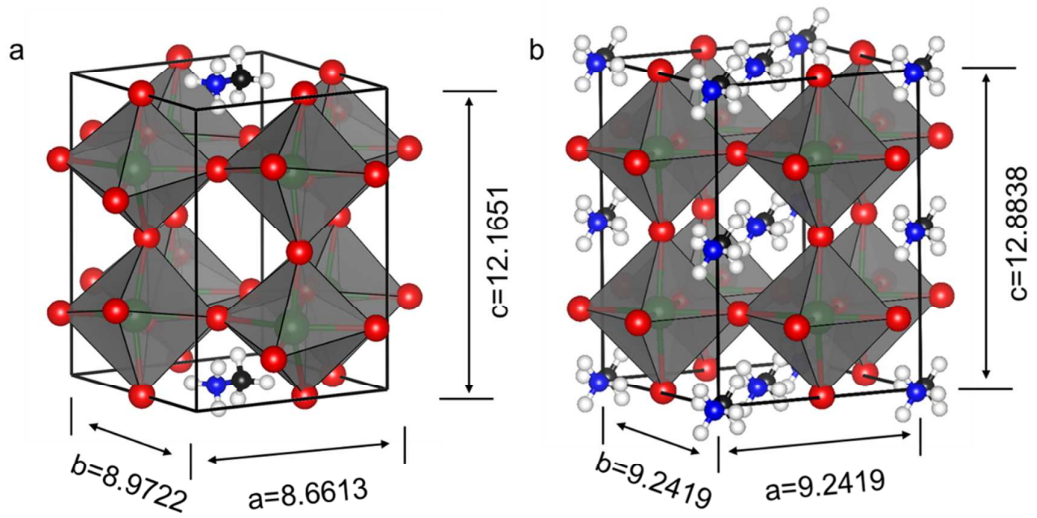

Figure S6 The relaxed structures for the tetragonal phase perovskite with different MA^+ intercalation ratios. (a) CH_3NH_3/Pb=0.25. (b) CH_3NH_3/Pb=1.

Table 1 The lattice constants of tetragonal perovskite ($AyBX_3$) with different intercalation ratios of CH_3NH_3.

y	Lattice type	Lattice parameters, *a*, *b* and *c* in Å
0.25	Monoclinic	*a*=8.6613, *b*=8.9722, *c*=12.1651, *α*=90.00°, *β*=90.00°, *γ*=86.43°
0.5		*a*=9.2047, *b*=8.9159, *c*=12.3357, *α*=90.00°, *β*=90.00°, *γ*=86.53°
0.75		*a*=8.9251, *b*=8.9608, *c*=12.6323, *α*=90.02°, *β*=90.29°, *γ*=89.35°
1	Tetragonal	*a*=*b*=9.2419, *c*=12.8838, *α*=*β*=*γ*=90.00°

All the calculations were performed by Vienna Ab-initio Simulation Package (VASP). Project augment wave (PAW) method was used to describe the interaction between the ion and valence electrons. The exchange-correlation functional developed by Perdew, Burke and Ernzerhof (PBE) was used. The energy cutoff of all the calculations was set to 500 eV. A Monkhorst-pack k-point mesh with density of 4×4×2 was used in the calculations of tetragonal phase. The tetragonal phase of ABX_3 was modelled by a $\sqrt{2}\times\sqrt{2}\times 2$ supercell of the cubic unit cell with four CH_3NH_3

molecules in it. To simulate the perovskite crystal structure with different CH_3NH_3 molecules, the corresponding numbers of CH_3NH_3 molecules were added from the simulation cell. In the initial structure, the C-N bond of all CH_3NH_3 molecules was set to align in the <100> direction of the cubic unit cell. Then all the structures were relaxed until the force exerted on each atom is less than 0.01 eV/Å^2.

The DFT calculations results (Figure S6) suggest that the crystal structure transforms from hexagonal to monoclinic system when the CH_3NH_3I molecules start to intercalate into the interval sites of PbI_6 octahedrons layers. However, due to the completely conversion of PbI_2 into $CH_3NH_3PbI_3$ perovskite, the length of *c*-axis could be increased and the shear stress in *a*-*b* plane will be introduced, which changes the γ angle. As a result, the lattice changes from monoclinic to tetragonal structure.

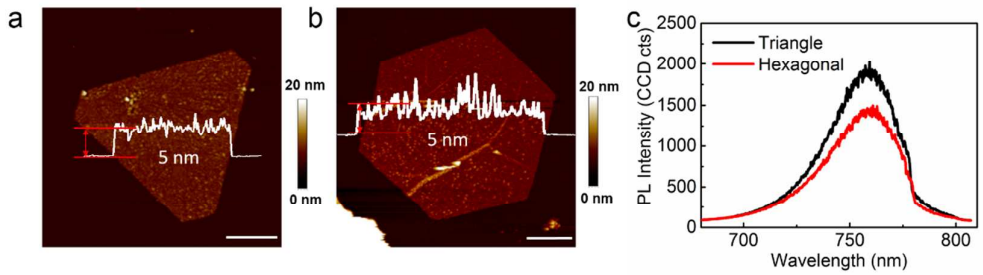

Figure S7 (a) and (b) AFM topography images of 2D $CH_3NH_3PbI_3$ nanosheets with the same thickness but different shapes (a: Triangle; b: Hexagon). Scale bars: 2 μm. (c) PL spectra collected from a and b.

Figure S7 a and b show the AFM topography image of the truncated triangular and hexagonal nanosheets with the same thickness. The PL spectra in Figure S7c are collected from the sample in a and b. It can be seen that these is no clear PL peak shift between these two spectra, indicating the same phase and structure. The intensity

difference of the PL spectra might be due to the different laser intensities, focusing conditions or integration times.

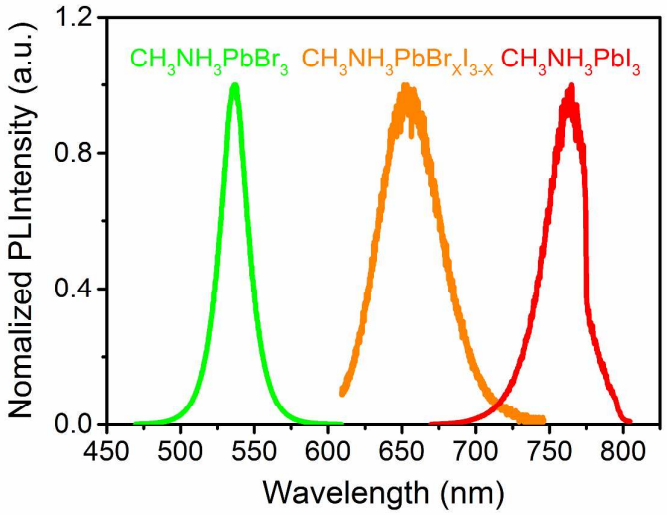

Figure S8 Nomalized PL spectra of 2D perovskite nanosheets with different compositions. Red trace: $CH_3NH_3PbI_3$; orange trace: $CH_3NH_3PbBr_xI_{3-x}$; green trace: $CH_3NH_3PbBr_3$.

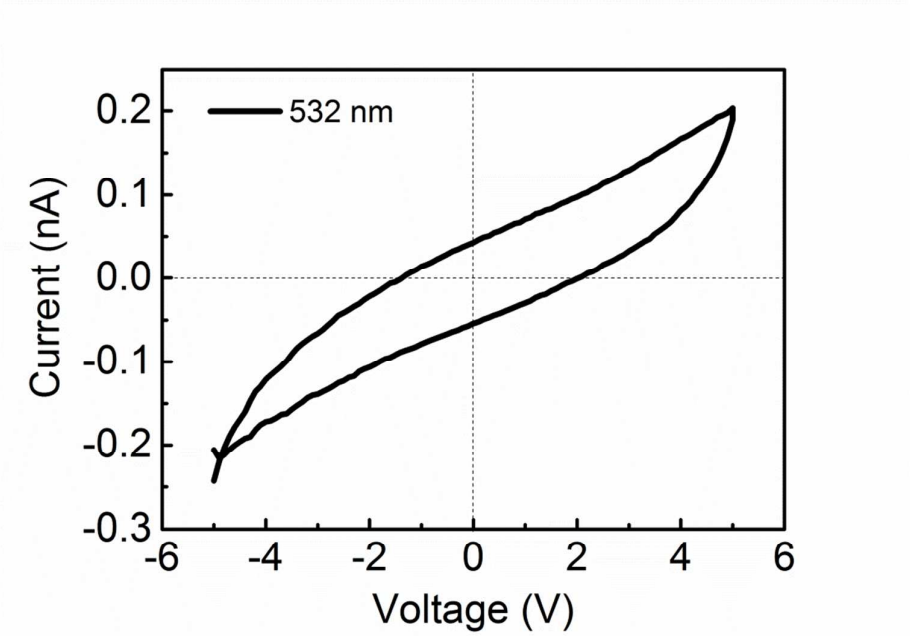

Figure S9 I-V curves of the 2D perovskite based device under the irradiation of weak unfocused 532 nm laser.

When the 2D perovskite based device was illuminated by weak laser (405 nm or 532 nm, unfocused, the effective power: <10 pw), the hysteresis can be observed in I-V curves, *i.e.* the current depends on the direction of the voltage sweeping between the source and drain electrodes. This means that some displacement (*i.e.* charge concentrations) related to the light intensity may happened, which could not be introduced by charge carriers injected from the contacts under forward bias.

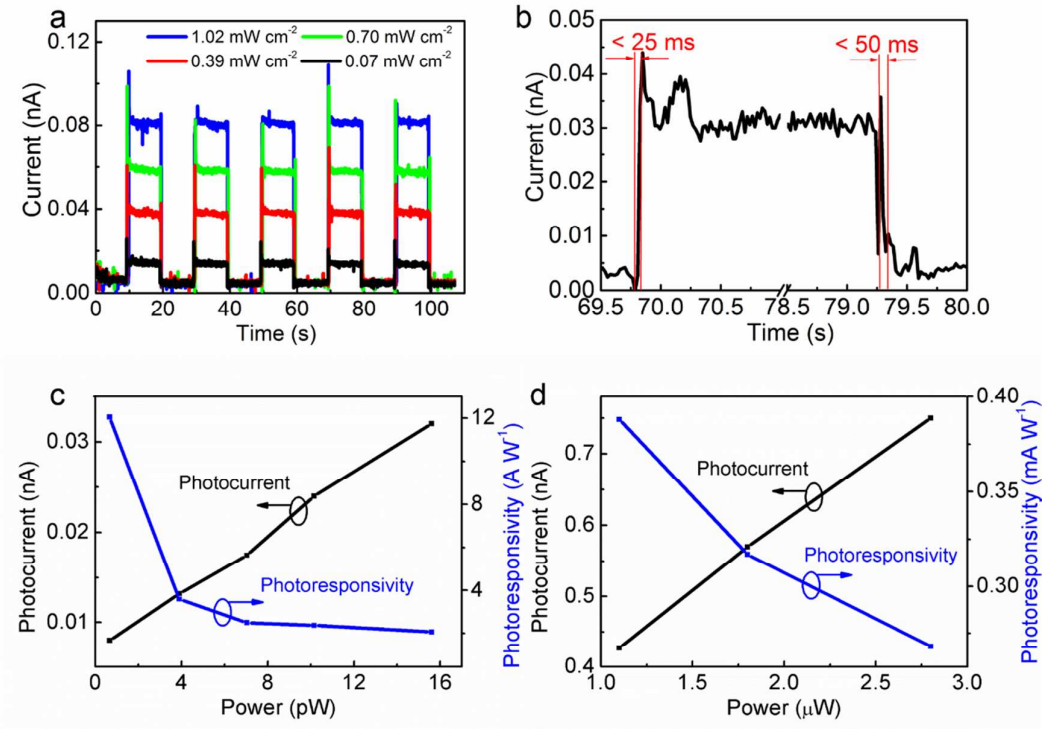

Figure S10 (a) Time-dependent photocurrent measurement on perovskite phototransistor over a five-period on- off operation under the different illumination of 532 laser. (b) Temporal photocurrent response excited at 532 nm. The rise time (< 25ms) is defined as the time for the photocurrent increased to 70% of ON-state current. The fall time (< 50ms) is defined as the time for the photocurrent decreased by 70% of ON-state current. (c) Photocurrent and photoresponsivity *versus* optical illumination power at a wavelength of 532 nm with a voltage bias of 1V. (d) Photocurrent and photoresponsivity *versus* optical illumination power under natural light with a voltage bias of 1V.

Figure S10a shows the photocurrent response of the device under the irradiation of the 532 nm laser with different power. Compared with the photocurrent response under the irradiation of the 405 nm laser, it can be found that the higher photocurrent was generated under 405 nm laser, in agree with the higher absorbance at a shorter wavelength. Temporal photocurrent response of the transistor under 532 nm laser was measured, as shown in figure S9b. The result reveals that a rise time less than 25 ms and a fall time less than 50 ms (70%), which can be applicable for many applications.

Figure S10c and d shows the dependence of photocurrent and photoresponsivity on 532nm laser (c) and natural light (d) with a voltage bias of 1V. The photocurrent is increased linearly with promoting the light power. It can be seen that higher photoresponsivity can be achieved when decreasing the illumination power.

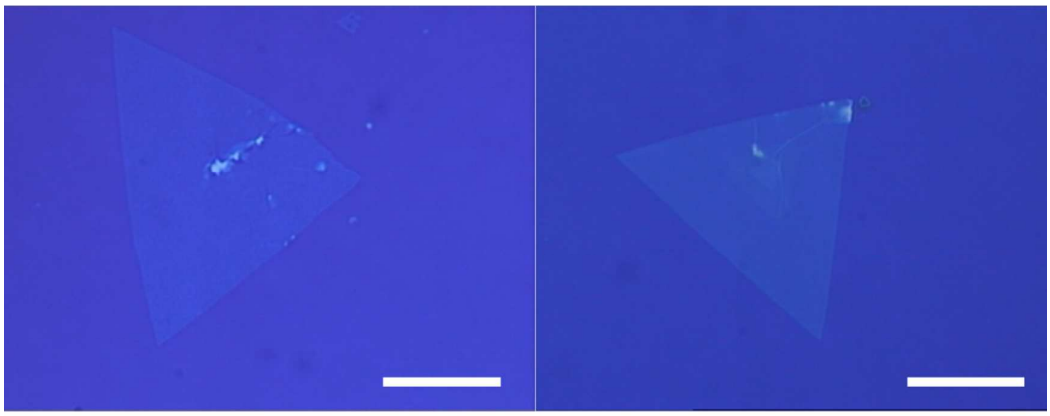

Figure S11. Optical images of larger size single crystal perovskite 2D nanosheets. Scale bars: 20 μm.